

AN EFFICIENT AND ACCURATE NUMERICAL METHOD FOR COMPUTING THE GROUND STATES OF THREE-DIMENSIONAL ROTATING DIPOLAR BOSE-EINSTEIN CONDENSATES UNDER STRONGLY ANISOTROPIC TRAP *

QINGLIN TANG[†], HANQUAN WANG[‡], SHAOBO ZHANG [†], AND YONG ZHANG[§]

Abstract. In this article, we propose an efficient and spectrally accurate numerical method to compute the ground states of three-dimensional (3D) rotating dipolar Bose-Einstein condensates (BEC) under strongly anisotropic trapping potentials. The kernel singularity, convolution non-locality and density anisotropy together complicate the dipolar potential evaluation. The fast rotation mechanism not only induces a complicated energy landscape with many local minima, but also creates a large number of vortices in the condensates. Such factors collectively make the ground state computation challenging in terms of convergence, accuracy and efficiency, especially for 3D anisotropic systems. Coupled with Fourier spectral discretization, we proposed a preconditioned conjugate gradient method (PCG) by integrating the anisotropic truncated kernel method (ATKM) for the dipolar potential evaluation. An adaptive step size control strategy is designed and ATKM allows for a spectral accuracy without introducing any extra anisotropy-dependent memory requirement or computational time. Our algorithm is spectrally accurate, highly efficient and memory-economic. Extensive numerical results are presented to confirm the accuracy and efficiency, together with applications to study impacts of the model parameters on critical rotational frequency, energies and chemical potential. Furthermore, these simulations reveal additional novel ground state patterns, such as bent vortices.

Key word. three-dimensional anisotropic rotating dipolar BEC, ground state, anisotropic truncated kernel method, preconditioned conjugate gradient method, bent vortices

1. Introduction. Since the first successful realization of Bose-Einstein condensates (BEC) in 1995 [4, 16, 18], the field has witnessed numerous significant advancements [13, 23, 41]. Notably, the introduction of the rotational frame gives rise to vortices [2, 25], while the long-range dipolar potential leads to intriguing phenomena such as magnetostriction [36] and the formation of quantum droplets [33] that can self-organize into supersolid phases [17, 32, 38]. Recently, microwave shielding technique has been utilized to suppress the two- and three-body losses in sodium-cesium molecules, and, for the first time, a dipolar molecular BEC has been achieved, which offers a clean and highly tunable system for strongly dipolar quantum matter and quantum simulation [14]. In addition, by breaking the symmetry of the confining potential, anisotropic traps serve as a versatile platform for investigating a wide range of fundamental mechanisms and properties, from the morphology of the quantum gas and anisotropic expansions [23] to the vortex arrangement [31] and quasiparticle excitations [41]. A remarkable finding is that *bent vortices* [2, 21, 22] were observed in the elongated rotating BEC with strong local interactions, which further inspired the

*This work was supported by the National Key R&D Program of China (No. 2024YFA1012803) (Q. Tang, S. Zhang and Y. Zhang), the Institutional Research Fund from Sichuan University (No. 2020SCUNL110) (Q. Tang and S. Zhang), the basic research fund of Tianjin University (No. 2025XJ21-0010) (Y. Zhang), the National Natural Science Foundation of China No.12271400 (S. Zhang and Y. Zhang) and No. 11871418, 11971120 (H. Wang), and Yunnan Fundamental Research Projects (No. 202101AS070044) (H. Wang).

[†]College of Mathematics, Sichuan University, No.24 South Section 1, Yihuan Road, Chengdu, China, 610065. (qinglin_tang@scu.edu.cn, shaobo_zhang@scu.edu.cn).

[‡]School of Statistics and Mathematics, Yunnan University of Finance and Economics, Kunming, Yunnan, China, 650221. (wang_hanquan@hotmail.com).

[§]Corresponding author. Center for Applied Mathematics and KL-AAGDM, Tianjin University, Tianjin, China, 300072. (Zhang_Yong@tju.edu.cn).

exploration of vortex lines. Given these advances, the study of rotating dipolar BEC under strongly anisotropic traps attracts great interest in the physics community, promising the emergence of further novel quantum phenomena.

At temperature T much smaller than the critical temperature T_c , the property of three-dimensional rotating dipolar BEC can be described by the complex-valued wave function $\psi(\mathbf{x}, t)$ whose evolution is governed by the dimensionless Gross-Pitaevskii equation (GPE) [8] as follows

$$(1.1) \quad i\partial_t \psi(\mathbf{x}, t) = \left[-\frac{1}{2}\nabla^2 + V(\mathbf{x}) + \beta|\psi|^2 + \lambda\Phi(\mathbf{x}, t) - \Omega L_z \right] \psi(\mathbf{x}, t),$$

$$(1.2) \quad \Phi(\mathbf{x}, t) = (U_{\text{dip}} * |\psi|^2)(\mathbf{x}, t),$$

$$(1.3) \quad \psi(\mathbf{x}, 0) = \psi_0(\mathbf{x}),$$

where t is the time variable and $*$ represents the convolution operator with respect to the spatial variable $\mathbf{x} = (x, y, z)^T \in \mathbb{R}^3$. The rotation term $L_z = -i(x\partial_y - y\partial_x) = -i\partial_\theta$ is the z -component of the angular momentum and Ω represents the rotational frequency. The dimensionless constant β describes the strength of short-range two-body interactions in a condensate, and $V(\mathbf{x})$ is a given real-valued external trapping potential which is determined by the system under investigation. In most BEC experiments, a harmonic potential is chosen to trap the condensate, i.e.,

$$(1.4) \quad V(\mathbf{x}) = \frac{1}{2}(\gamma_x^2 x^2 + \gamma_y^2 y^2 + \gamma_z^2 z^2),$$

where $\gamma_x > 0$, $\gamma_y > 0$ and $\gamma_z > 0$ are dimensionless constants proportional to the trapping frequencies in the x -, y - and z -direction, respectively. The trapping potential is isotropic if $\gamma_x = \gamma_y = \gamma_z$, and is anisotropic otherwise. The system is considered strongly anisotropic when maximum of the trapping frequency ratio is great than 1, i.e., $\max_{i,j=x,y,z} \{\gamma_i/\gamma_j\} \gg 1$. Moreover, λ is a constant characterizing the strength of dipolar potential and $U_{\text{dip}}(\mathbf{x})$ is the dipole-dipole interaction kernel defined as

$$(1.5) \quad U_{\text{dip}}(\mathbf{x}) = \frac{3}{4\pi|\mathbf{x}|^3} \left[1 - \frac{3(\mathbf{x} \cdot \mathbf{n})^2}{|\mathbf{x}|^2} \right] = -\delta(\mathbf{x}) - 3\partial_{\mathbf{n}\mathbf{n}} \left(\frac{1}{4\pi|\mathbf{x}|} \right), \quad \mathbf{x} \in \mathbb{R}^3,$$

with dipole orientation $\mathbf{n} = (n_1, n_2, n_3)^T$ being a given unit vector, i.e., $|\mathbf{n}| = \sqrt{n_1^2 + n_2^2 + n_3^2} = 1$, $\partial_{\mathbf{n}} = \mathbf{n} \cdot \nabla$ and $\partial_{\mathbf{n}\mathbf{n}} = \partial_{\mathbf{n}}(\partial_{\mathbf{n}})$. In fact, for smooth densities $\rho(\mathbf{x}) := |\psi(\mathbf{x})|^2$, the dipolar potential can be reformulated via 3D Coulomb potential as follows

$$(1.6) \quad \Phi(\mathbf{x}) = -\rho - 3 \frac{1}{4\pi|\mathbf{x}|} * (\partial_{\mathbf{n}\mathbf{n}}\rho) := -\rho - 3 [U * (\partial_{\mathbf{n}\mathbf{n}}\rho)], \quad U(\mathbf{x}) = \frac{1}{4\pi|\mathbf{x}|},$$

where $U(\mathbf{x})$ is the three-dimensional Coulomb interaction kernel. The time-dependent GPE (1.1)–(1.3) conserves two important quantities: the *total mass* (or normalization) of the wave function

$$(1.7) \quad N(\psi(\cdot, t)) := \|\psi(\cdot, t)\|_{L^2}^2 = \int_{\mathbb{R}^3} |\psi(\mathbf{x}, t)|^2 d\mathbf{x} \equiv 1, \quad t \geq 0,$$

and the *energy per particle*

$$(1.8) \quad E(\psi(\cdot, t)) := \int_{\mathbb{R}^3} \left(\frac{1}{2} |\nabla \psi|^2 + V(\mathbf{x})|\psi|^2 + \frac{\beta}{2} |\psi|^4 + \frac{\lambda}{2} \Phi |\psi|^2 - \Omega \bar{\psi} L_z \psi \right) d\mathbf{x} \equiv E(\psi(\cdot, 0)),$$

where $\bar{\psi}$ is the conjugate of ψ .

To find a stationary solution of Eq. (1.1), we write $\psi(\mathbf{x}, t) = \phi(\mathbf{x})e^{-i\mu t}$, where μ is the chemical potential of the condensate and $\phi(\mathbf{x})$ is the stationary state. Plugging it into (1.1), we obtain

$$(1.9) \quad \mu \phi(\mathbf{x}) = \left[-\frac{1}{2}\nabla^2 + V(\mathbf{x}) + \beta|\phi|^2 + \lambda (U_{\text{dip}} * |\phi|^2) - \Omega L_z \right] \phi(\mathbf{x}).$$

This is indeed a nonlinear eigenvalue problem under a normalization constraint $N(\phi) = 1$, and any eigenvalue μ can be computed from its corresponding eigenfunction ϕ by

$$\begin{aligned} \mu &= \int_{\mathbb{R}^3} \left(\frac{1}{2}|\nabla\phi|^2 + V(\mathbf{x})|\phi|^2 + \beta|\phi|^4 + \lambda (U_{\text{dip}} * |\phi|^2) |\phi|^2 - \Omega\bar{\phi}L_z\phi \right) d\mathbf{x} \\ &= E(\phi) + \int_{\mathbb{R}^3} \left(\frac{\beta}{2}|\phi|^4 + \frac{\lambda}{2} (U_{\text{dip}} * |\phi|^2) |\phi|^2 \right) d\mathbf{x}. \end{aligned}$$

Equivalently, the stationary states ϕ are critical points of the energy functional $E(\phi)$ over the unit sphere $\mathcal{S} := \{\phi(\mathbf{x}) \mid \|\phi\|_{L^2}^2 = 1, E(\phi) < \infty\}$. The ground state ϕ_g is defined as the minimizer of the energy functional $E(\phi)$:

$$(1.10) \quad \phi_g = \arg \min_{\phi \in \mathcal{S}} E(\phi).$$

The existence of ground state in rotating dipolar BEC has been well-studied theoretically [8]. When the trapping potential is strongly anisotropic, e.g., pancake-shaped or cigar-shaped, the three-dimensional system can be approximated by a two/one-dimensional model [11]. However, a gap persists between such low-dimensional approximations and physical systems, especially in regimes of intermediate anisotropy. Importantly, some physical phenomena, such as vortex lines in rotating BEC, can only be observed in three-dimensional space. It is therefore essential to resort to the original three-dimensional model, despite the inevitably high computational costs involved. To date, few numerical methods have been developed to compute the ground state of rotating dipolar BEC in strongly anisotropic regimes.

For numerical study on the ground state of anisotropic rotating dipolar BEC, there are three challenges: (i) The strongly anisotropic trap introduces vastly different scales of variation along each direction, demanding sufficiently high resolution in all directions to capture fine structures. (ii) The singular kernel and the anisotropic density pose significant challenges to evaluating the dipolar potential with both accuracy and efficiency. (iii) Fast rotation induces the formation of quantum vortices and creates an intricate energy landscape with many local minima [35], which complicates the computation of the ground state.

In presence of a confining anisotropic potential $V(\mathbf{x})$, the wave function ψ (density ρ) is smooth, fast-decaying and anisotropic. Thus, it suffices to truncate the whole space to an anisotropic rectangular domain

$$(1.11) \quad \mathcal{D}_{L\xi} := \prod_{\alpha} [-L\xi_{\alpha}, L\xi_{\alpha}], \quad 0 < \xi_{\alpha} \leq 1, \quad \alpha = x, y, z,$$

with $\xi_{\alpha} = 1$ on the longest side of $\mathcal{D}_{L\xi}$. The truncated domain is then discretized with uniform mesh grid in each spatial direction. The anisotropy vector and strength are defined as

$$(1.12) \quad \boldsymbol{\xi} = (\xi_x, \xi_y, \xi_z)^T, \quad \xi_f = 1/(\xi_x\xi_y\xi_z)$$

respectively. For readers' convenience, we present graphical illustrations of the anisotropic computation domains with $\xi = (\frac{1}{10}, \frac{1}{10}, 1)^T$ (cigar-shape) and $\xi = (1, 1, \frac{1}{10})^T$ (pancake-shape) in Fig. 1. The wave function (density) is well approximated by the



Fig. 1: Schematic diagrams of cigar- and pancake-shape domain $\mathcal{D}_{L\xi}$ with $\xi = (\frac{1}{10}, \frac{1}{10}, 1)^T$ (left) and $\xi = (1, 1, \frac{1}{10})^T$ (right).

Fourier spectral method [8, 34], which helps achieve spectral accuracy with $\mathcal{O}(N \log N)$ efficiency thanks to the discrete Fast Fourier Transform (FFT). To capture fine structures such as vortex lattices, the mesh size should be small enough, which usually leads to a large system and consequently severe memory and computational costs.

Due to kernel singularity, convolution non-locality and density anisotropy, it is challenging to compute the dipolar potential with spectral accuracy while maintaining the FFT-like efficiency. During the last decade, several fast spectral methods have been proposed, including the NonUniform Fast Fourier Transform method (NUFFT) [26], Gaussian-Summation method (GauSum) [20], Kernel Truncation Method (KTM) [39] and Anisotropic Truncated Kernel Method (ATKM)[24]. All these methods achieve similar spectral accuracy but differ in terms of efficiency, particularly in cases where the density is strongly anisotropic. For NUFFT and KTM, the memory requirement and efficiency performance depend linearly on the anisotropy strength, therefore, they can hardly handle the strongly anisotropic case. The GauSum method splits the potential into one regular and singular integral, and costs more computation time than ATKM. In this article, we adopt ATKM, which is introduced by Greengard *et al.* [24] to especially deal with the anisotropic density via rectangular instead of circular extension of the computation domain $\mathcal{D}_{L\xi}$ (1.11). The memory requirement and efficiency of ATKM are independent of the anisotropy strength, which guarantees excellent performance even when the density function is strongly anisotropic.

For the computation of the ground state, there have been many methods proposed based on imaginary-time evolution [8, 10, 9, 12]. For fast rotating BEC, these methods often exhibit slow convergence, making it impractical to obtain the ground state within an affordable computational time. Alternatively, the ground state can also be obtained by solving a constrained nonlinear eigenvalue problem, which actually corresponds to an optimization problem defined on a Riemannian manifold [3, 19]. It is quite natural to apply the state-of-art Riemannian optimization techniques [1, 15] therein. For example, a preconditioned conjugate gradient algorithm (PCG), proposed [5] for the rotating BEC, has greatly accelerated the convergence and significantly improved the efficiency. The ground state of rotating dipolar BEC has been investigated by combing PCG with KTM [6] for normal isotropic trapping potentials. For the BEC under strongly anisotropic traps, the aforementioned method is hardly practical due to the huge memory burden and long computational time brought in by the usage of KTM for the dipolar potential evaluation.

Regarding all the above aspects, in this article, we aim to propose a preconditioned

conjugate gradient algorithm by combining ATKM for dipolar potential evaluation. By designing an appropriate step size control strategy and addressing the challenge arising from integration of PCG and ATKM, our method achieves spectral accuracy with high efficiency, and more importantly, the memory requirement is independent of the anisotropy strength. Then, we study bent vortices in the dipolar BEC under different parameter setups (Subsection 3.2), and these results confirm the importance and necessity of our algorithm for handling such strongly anisotropic dipolar systems. In addition, using our algorithm, we identify novel ground state patterns and comprehensively investigate the impacts of model parameters on the critical rotational frequency and energies.

The rest of the paper is organized as follows: In Section 2, we introduce the spatial discretization by Fourier spectral method and a brief review of the ATKM for dipolar potential evaluation, and then propose an accurate and efficient numerical algorithm by integrating PCG with ATKM. In Section 3, we present extensive numerical results to confirm the accuracy and efficiency, along with applications to investigate the impacts of model parameters on critical rotational frequency, energies and chemical potential. Moreover, we identify some ground state patterns and study the bent vortices in dipolar BEC. Finally, some conclusions are drawn in Section 4.

2. Numerical algorithm. Here we first utilize the Fourier spectral method [34] to discretize the wave function ϕ on domain $\mathcal{D}_{L\xi}$ (1.11). Then, we present a detailed introduction of ATKM for evaluating dipolar potentials, and propose an accurate and efficient numerical method to compute the ground state of rotating dipolar BEC under anisotropic traps.

2.1. Spatial discretization. The computation domain $\mathcal{D}_{L\xi}$ is discretized along each spatial direction with mesh size $h_\alpha = 2L\xi_\alpha/N_\alpha$, where N_α ($\alpha = x, y, z$) are even positive integers, and the total grid number is denoted as $N = N_x N_y N_z$. For simplicity, we denote the mesh size vector $\mathbf{h} := (h_x, h_y, h_z)$, grid number vector $\mathbf{N} := (N_x, N_y, N_z)$ and mesh grids $\mathbf{x}_j := (x_{j_x}, y_{j_y}, z_{j_z})$. The set of mesh grids is defined as

$$\mathcal{T} := \{\mathbf{x}_j = (-L\xi_x + j_x h_x, -L\xi_y + j_y h_y, -L\xi_z + j_z h_z), \mathbf{j} \in \mathcal{I}_{\mathbf{N}}\},$$

with index set

$$\mathcal{I}_{\mathbf{N}} := \{\mathbf{j} = (j_x, j_y, j_z) \in \mathbb{N}^3 \mid 0 \leq j_\alpha \leq N_\alpha - 1, \alpha = x, y, z\}.$$

We denote f_j as the numerical approximation of $f(\mathbf{x}_j)$, $\mathbf{x}_j \in \mathcal{T}$ and f as the vector with components $\{f_j\}_{j \in \mathcal{I}_{\mathbf{N}}}$. Moreover, we introduce the Fourier index set

$$\Lambda_{\mathbf{N}} := \{\mathbf{k} := (k_x, k_y, k_z) \in \mathbb{Z}^3 \mid -N_\alpha/2 \leq k_\alpha \leq N_\alpha/2 - 1, \alpha = x, y, z\},$$

and define the Fourier basis function as

$$W_{\mathbf{k}}^L(\mathbf{x}) := e^{i\nu_{k_x}(x+L\xi_x)} e^{i\nu_{k_y}(y+L\xi_y)} e^{i\nu_{k_z}(z+L\xi_z)}, \quad \nu_{k_\alpha} = \pi k_\alpha / (L\xi_\alpha), \quad \mathbf{k} \in \Lambda_{\mathbf{N}}.$$

The Fourier spectral approximation of wave function ϕ on domain $\mathcal{D}_{L\xi}$ reads as

$$(2.1) \quad \phi(\mathbf{x}) \approx \sum_{\mathbf{k} \in \Lambda_{\mathbf{N}}} \widehat{\phi}_{\mathbf{k}} W_{\mathbf{k}}^L(\mathbf{x}), \quad \mathbf{x} \in \mathcal{D}_{L\xi},$$

where $\widehat{\phi}_{\mathbf{k}}$, the discrete Fourier coefficients, are given by

$$(2.2) \quad \widehat{\phi}_{\mathbf{k}} := \frac{1}{N} \sum_{j \in \mathcal{I}_{\mathbf{N}}} \phi_j \overline{W_{\mathbf{k}}^L(\mathbf{x}_j)}.$$

The above summation can be accelerated by FFT within $\mathcal{O}(N \log N)$ operations. In fact, the approximation (2.1) is actually an interpolation function at mesh grid points $\mathbf{x}_j \in \mathcal{T}$. We approximate $\partial_x \phi$, $\Delta \phi$ and $L_z \phi$ on mesh \mathcal{T} by differentiating the corresponding finite Fourier series (2.1) as follows:

$$(2.3) \quad \begin{aligned} (\partial_x \phi)_j &\approx ([\partial_x] \phi)_j = \sum_{\mathbf{k} \in \Lambda_N} (i\nu_{k_x}) \widehat{\phi}_{\mathbf{k}} W_{\mathbf{k}}^L(\mathbf{x}_j), \\ (\Delta \phi)_j &\approx ([\Delta] \phi)_j = \sum_{\mathbf{k} \in \Lambda_N} \left(- \sum_{\alpha=x,y,z} (\nu_{k_\alpha})^2 \right) \widehat{\phi}_{\mathbf{k}} W_{\mathbf{k}}^L(\mathbf{x}_j), \\ (L_z \phi)_j &\approx ([L_z] \phi)_j = -i(x[\partial_y] \phi - y[\partial_x] \phi)_j. \end{aligned}$$

2.2. Anisotropic truncated kernel method. To evaluate the dipolar potential, it is clear that direct discretization of the convolution integral might diverge when the source and target points coincide, so special treatment is required to deal with such singularity that is caused by the singular but integrable convolution kernel. Numerical schemes based on direct integral discretization, whose computation complexity is about $\mathcal{O}(N^2)$ flops, are often too time-consuming and become even impractical for high-dimensional problems since the total grid number N will easily soar to millions or billions. Moreover, under a strongly anisotropic trap, the density function exhibits a strong spatial anisotropy. That is to say, the span of its compact support in one or two spatial directions is much shorter than those in the other directions. Such anisotropic density will aggravate the computation difficulty. Here we choose the fast spectral solver ATKM [24], which is particularly designed to evaluate convolution-type nonlocal potentials with anisotropic densities. As shown in Eq. (1.6), the dipolar potential can be rewritten as a summation of the density and a Coulomb potential generated by $\partial_{nn}\rho(\mathbf{x})$.

Since the density ρ is smooth, anisotropic and decays exponentially fast, it is reasonable to assume that ρ is compactly supported in an anisotropic rectangular domain $\mathcal{D}_{L\xi}$. The potential on $\mathcal{D}_{L\xi}$ now reads

$$(2.4) \quad \begin{aligned} \Phi(\mathbf{x}) &= \int_{\mathbb{R}^3} U(\mathbf{y}) \rho(\mathbf{x} - \mathbf{y}) d\mathbf{y} = \int_{\mathbf{x} + \mathcal{D}_{L\xi}} U(\mathbf{y}) \rho(\mathbf{x} - \mathbf{y}) d\mathbf{y}, \\ &= \int_{\mathcal{D}_{2L\xi}} U(\mathbf{y}) \rho(\mathbf{x} - \mathbf{y}) d\mathbf{y}, \quad \mathbf{x} \in \mathcal{D}_{L\xi}. \end{aligned}$$

The third equation holds because, for any $\mathbf{x} \in \mathcal{D}_{L\xi}$, $\mathbf{y} \in \mathcal{D}_{2L\xi} \setminus (\mathbf{x} + \mathcal{D}_{L\xi})$, we have $\mathbf{x} - \mathbf{y} \notin \mathcal{D}_{L\xi}$ and thus $\rho(\mathbf{x} - \mathbf{y}) = 0$. To integrate Eq. (2.4), we need to approximate the density ρ on domain $\mathcal{D}_{3L\xi}$, because $\mathbf{x} - \mathbf{y} \in \mathcal{D}_{3L\xi}$ for any $\mathbf{x} \in \mathcal{D}_{L\xi}$ and $\mathbf{y} \in \mathcal{D}_{2L\xi}$. It is natural to extend the density to $\mathcal{D}_{3L\xi}$ by zero-padding and apply the Fourier spectral method therein. Fortunately, it is sufficient to approximate the density on a *twofold* domain $\mathcal{D}_{2L\xi}$ thanks to the periodicity of Fourier series, and we refer to [24, 20] for more details.

The density ρ is well resolved by the following Fourier spectral method

$$(2.5) \quad \rho(\mathbf{z}) \approx \sum_{\mathbf{k} \in \Lambda_{2N}} \widehat{\rho}_{\mathbf{k}} W_{\mathbf{k}}^{2L}(\mathbf{z}), \quad \mathbf{z} \in \mathcal{D}_{2L\xi},$$

where the discrete Fourier coefficients $\widehat{\rho}_{\mathbf{k}}$ are given below

$$(2.6) \quad \widehat{\rho}_{\mathbf{k}} := \frac{1}{8N} \sum_{j \in \mathcal{I}_{2N}} \rho_j \overline{W_{\mathbf{k}}^{2L}(\mathbf{z}_j)}.$$

Plugging (2.5) into (2.4), we obtain

$$(2.7) \quad \Phi(\mathbf{x}) \approx \sum_{\mathbf{k} \in \Lambda_{2N}} \widehat{U}_{\mathbf{k}} \widehat{\rho}_{\mathbf{k}} W_{\mathbf{k}}^{2L}(\mathbf{x}), \quad \mathbf{x} \in \mathcal{D}_{L\xi},$$

where $\widehat{U}_{\mathbf{k}}$, the Fourier coefficients of kernel $U(\mathbf{y})$ on domain $\mathcal{D}_{2L\xi}$, are defined below

$$(2.8) \quad \widehat{U}_{\mathbf{k}} := \int_{\mathcal{D}_{2L\xi}} U(\mathbf{y}) \overline{W_{\mathbf{k}}^{2L}(\mathbf{y})} \, d\mathbf{y}.$$

The above singular Fourier integral is actually well-defined, and Greengard *et al.* proposed an efficient and accurate algorithm to evaluate it based on a black-box sum-of-Gaussians approximation of the symmetric kernel $U(\mathbf{y})$ [24]. By taking advantage of the separable structure of Gaussian functions, the Fourier coefficients $\widehat{U}_{\mathbf{k}}$ can be calculated within $\mathcal{O}(N)$ operations. Clearly, once $\widehat{U}_{\mathbf{k}}$ is available, the nonlocal potential computation (2.7) can be accomplished in three simple steps: (1) compute the discrete Fourier coefficient $\widehat{\rho}_{\mathbf{k}}$ (2.6) via FFT; (2) compute $\widehat{U}_{\mathbf{k}} \widehat{\rho}_{\mathbf{k}}$ by pointwise function multiplication and (3) compute $\Phi(\mathbf{x}_j)$ via inverse FFT. The total computational costs amount to $\mathcal{O}(2^3 N \log(2^3 N))$.

As mentioned above, the density anisotropy property is taken into account at the very beginning by taking an anisotropic rectangular domain and carrying out a twofold anisotropic extension. Once the computation of $\widehat{U}_{\mathbf{k}}$ (2.8), which is a Fourier integral defined on the anisotropic domain too, is available, the potential is computed via a pair of FFT/iFFT on vectors of twofold length in each spatial direction. Thus, both the computational time and memory requirement are *independent* of the anisotropy strength ξ_f (1.12). While, for KTM, the total optimal zero-padding factor linearly depends on the anisotropy strength [28], and the precomputation of Fourier coefficients suffers badly from prohibitive memory requirement and computational costs in high dimensions.

REMARK 1. *To provide a vivid illustration of the comparison between KTM and ATKM, we consider a double-precision computation with an anisotropy vector $\boldsymbol{\xi} = (\frac{1}{10}, \frac{1}{10}, 1)^T$. Here we compare the memory requirement of Fourier coefficients $\widehat{U}_{\mathbf{k}}$. Given a uniform mesh with grid number $N = 256^3$, it requires only $256^3 \times 2^3 \times 8/2^{30} \text{ Gb} = 1 \text{ Gb}$ memory for ATKM. In contrast, the memory costs of KTM, whose total optimal zero-padding factor [39] amounts to 432, soars as much as **54 Gb**, which is far beyond most personal computers' capacity. In other words, the reduction factor on memory requirement is $1 - \frac{8}{432} \approx 98\%$.*

REMARK 2. *In simulation, the nonlocal potentials are often called multiple times with the same numerical setups, that is, both the domain and mesh grid are fixed. Therefore, the evaluation of $\widehat{U}_{\mathbf{k}}$ is computed once for all in the precomputation step.*

2.3. Ground state computation. Preconditioned conjugate gradient methods have been established for computing the ground states of rotating BEC with/without dipolar potential [5, 6, 43]. While their efficiency is well-established, existing approaches are designed under either isotropic or weakly anisotropic traps. For the most challenging strongly anisotropic regime, we develop a preconditioned conjugate gradient method that incorporates ATKM for dipolar potential evaluation to compute the ground state, addressing the difficulties existing in the subtle vortex-structure ground state caused by fast rotation, the normalization constraint and dipolar potential under a strongly anisotropic trap.

Based on the spatial discretization by Fourier pseudo-spectral method in subsection 2.1, we discretize the energy $E(\phi)$ on mesh grid \mathcal{T} as follows

$$(2.9) \quad E(\phi) \approx \mathcal{E}(\phi) = \left\langle -\frac{1}{2}[[\Delta]]\phi + V \odot \phi + \frac{\beta}{2}|\phi|^2 \odot \phi + \frac{\lambda}{2}[[\Phi]] \odot \phi - \Omega[[L_z]]\phi, \phi \right\rangle,$$

where $[[\Phi]]$ is the numerical approximation of Φ , \odot denotes Hadamard product and

$$(2.10) \quad \langle U, V \rangle := \Re \left(h_x h_y h_z \sum_{j \in \mathcal{I}_N} U_j \bar{V}_j \right), \quad \forall U, V \in \mathbb{C}^N,$$

is the inner product defined on \mathbb{C}^N with $\Re(\cdot)$ representing the real part of a complex number. The minimization problem (1.10) is then discretized into the finite dimensional minimization problem

$$(2.11) \quad \phi_g = \arg \min_{\phi \in \mathbb{S}} \mathcal{E}(\phi), \quad \mathbb{S} := \{\phi \in \mathbb{C}^N \mid \|\phi\| = 1\},$$

with norm $\|U\| = \langle U, U \rangle^{\frac{1}{2}}$.

The (Euclidean) gradient of energy $\mathcal{E}(\phi)$ on \mathbb{C}^N is

$$(2.12) \quad \begin{aligned} \nabla \mathcal{E}(\phi) &= 2H_\phi \phi, \\ H_\phi \phi &= -\frac{1}{2}[[\Delta]]\phi + V \odot \phi + \beta|\phi|^2 \odot \phi + \lambda[[\Phi]] \odot \phi - \Omega[[L_z]]\phi. \end{aligned}$$

The tangent space at a point $\phi \in \mathbb{S}$ is defined as $T_\phi \mathbb{S} := \{f \in \mathbb{C}^N \mid \langle f, \phi \rangle = 0\}$. And the orthogonal projection $J_\phi(f)$ from \mathbb{C}^N onto the tangent space $T_\phi \mathbb{S}$ is given by

$$(2.13) \quad J_\phi(f) := f - \langle f, \phi \rangle \phi.$$

The Riemannian gradient of energy on \mathbb{S} is

$$(2.14) \quad \nabla_{\mathbb{S}} \mathcal{E}(\phi) = J_\phi(\nabla \mathcal{E}(\phi)) = 2(H_\phi \phi - \mu_\phi \phi) \quad \text{with} \quad \mu_\phi = \langle H_\phi \phi, \phi \rangle.$$

The first-order necessary optimality condition states that at a minimum $\phi \in \mathbb{S}$, the gradient of the energy vanishes on the constraint manifold \mathbb{S} , i.e., $\nabla_{\mathbb{S}} \mathcal{E}(\phi) = 0$. This condition is indeed the Euler-Lagrange equation associated with problem (2.11):

$$(2.15) \quad H_\phi \phi = \mu_\phi \phi.$$

Further, the preconditioned conjugate gradient method on manifold \mathbb{S} is proposed.

To numerically solve the minimization problem (2.11), we denote the abstract grid function f of the n -th step as f_n . Moving from ϕ_n along a descent direction p_n on the manifold \mathbb{S} , we use the retraction

$$(2.16) \quad \phi_{n+1} = R_{\phi_n}(t_n p_n) := \cos(t_n \|p_n\|) \phi_n + \sin(t_n \|p_n\|) p_n / \|p_n\|,$$

with $p_n \in T_{\phi_n} \mathbb{S}$ and step size $t_n > 0$ (to be determined later). Regarding the direction p_n , we first introduce the tangent bundle of \mathbb{S} as $T\mathbb{S} := \cup_{\phi \in \mathbb{S}} T_\phi \mathbb{S}$. The transport operator $\mathcal{V} : T\mathbb{S} \times T\mathbb{S} \rightarrow T\mathbb{S}$, given explicitly below

$$\mathcal{V}_u(v) := J_{R_\phi(u)}(v) = v - \langle v, R_\phi(u) \rangle R_\phi(u), \quad \forall u \in T_\phi \mathbb{S}, v \in T_\phi \mathbb{S},$$

maps vector $v \in T_\varphi \mathbb{S}$ at point φ to tangent space at point $R_\phi(u) \in \mathbb{S}$. Specifically, for $p_{n-1} \in T_{\phi_{n-1}} \mathbb{S}$ and $v \in T_{\phi_{n-1}} \mathbb{S}$, we have $\mathcal{V}_{t_{n-1} p_{n-1}}(v) = J_{\phi_n}(v)$. Then the direction of conjugate gradient method is chosen as

$$(2.17) \quad p_n = \begin{cases} J_{\phi_n}(-Pr_n), & n = 0, \\ J_{\phi_n}(-Pr_n) + \beta_n^{cg} \mathcal{V}_{t_{n-1} p_{n-1}}(p_{n-1}) = J_{\phi_n}(-Pr_n) + \beta_n^{cg} J_{\phi_n}(p_{n-1}), & n > 0, \end{cases}$$

with the residual $r_n = \nabla_{\mathbb{S}} \mathcal{E}(\phi_n)/2 = H_{\phi_n} \phi_n - \mu_{\phi_n} \phi_n$. The parameter β_n^{cg} is given by Polak-Ribière choice [1]

$$(2.18) \quad \begin{aligned} \beta_n^{cg} &= \max(\beta_n^{PR}, 0), \\ \beta_n^{PR} &= \langle r_n - J_{\phi_n}(r_{n-1}), J_{\phi_n}(Pr_n) \rangle / \langle r_{n-1}, J_{\phi_{n-1}}(Pr_{n-1}) \rangle. \end{aligned}$$

The preconditioner P is a symmetric positive definite operator to help accelerate the convergence of iteration, which is given by [6]

$$(2.19) \quad P = P_V^{1/2} P_\Delta P_V^{1/2},$$

where P_Δ and P_V are respectively read as

$$(2.20) \quad \begin{aligned} P_\Delta &= (\alpha_\Delta - \llbracket \Delta \rrbracket / 2)^{-1}, \\ P_V &= (\alpha_V + V + \beta |\phi_n|^2 + |\lambda| (1 + \text{sign}(\llbracket \Phi_n \rrbracket)) \llbracket \Phi_n \rrbracket / 2)^{-1}, \end{aligned}$$

with α_Δ and α_V being positive shift constants, and here we take

$$(2.21) \quad \alpha_\Delta = \alpha_V = \langle -\frac{1}{2} \llbracket \Delta \rrbracket \phi_n + V \odot \phi_n + \beta |\phi_n|^2 \odot \phi_n, \phi_n \rangle + |\lambda| \langle \llbracket \Phi_n \rrbracket \odot \phi_n, \phi_n \rangle > 0.$$

This combined preconditioner achieves nearly optimal convergence performance, whose iteration number is independent of the computation domain and mesh size. For more details, we refer readers to [5, 6].

To find t_n in Eq. (2.16), we solve the nonlinear minimization problem

$$(2.22) \quad t_n = \arg \min_{t > 0} Q(t), \quad Q(t) := \mathcal{E}(R_{\phi_n}(t p_n)),$$

by utilizing a standard one-dimensional minimization algorithm. Since the exact line search is time-consuming, we introduce the following approximation method to obtain a simple and much cheaper approximation of t_n . Now that the retraction (2.16) is of second order accuracy, we expand $Q(t)$ as follows

$$(2.23) \quad Q(t) \approx \mathcal{E}(\phi_n) + 2t \langle H_{\phi_n} \phi_n, p_n \rangle + t^2 (\langle H_{\phi_n} p_n, p_n \rangle + \langle g_n, p_n \rangle - \mu_{\phi_n} \|p_n\|^2),$$

with $g_n = 2\phi_n (\beta \Re(\bar{\phi}_n p_n) + \lambda U * \Re(\bar{\phi}_n p_n))$. Note that $\langle H_{\phi_n} \phi_n, p_n \rangle$ may not be negative, so the direction p_n might not be a descent direction and the energy might not decrease. To select an appropriate step size t_n , we follow this procedure: (i) We check whether the coefficient of the first-order term is negative or not. If so, we choose the conjugate gradient direction and keep β_n^{cg} unchanged; otherwise, we employ the preconditioned steepest descent (PSD) method [5], i.e., we set $\beta_n^{cg} = 0$ so to ensure that $\langle H_{\phi_n} \phi_n, p_n \rangle < 0$ given that the preconditioner P is positive definite. (ii) We check further whether the coefficient of the second-order term is positive or not. If so, minimizing (2.23) with respect to t yields

$$(2.24) \quad t_n^{\text{app}} = - \langle H_{\phi_n} \phi_n, p_n \rangle / (\langle H_{\phi_n} p_n, p_n \rangle + \langle g_n, p_n \rangle - \mu_{\phi_n} \|p_n\|^2).$$

If not, we set the step size to a default value, i.e., $t_n = 0.3$. (iii) We then check whether the energy of ϕ_{n+1} decreases or not. If so, we accept the step size; otherwise, we decrease it by half until the energy decreases. The above process guarantees the energy decay property.

For the convenience of readers, the proposed method for solving the minimization problem (1.10) is summarized in **Algorithm 2.1**, which we refer to as PCG-ATKM. In this paper, we adopt the following stopping criterion

$$(2.25) \quad \|\phi_{n+1} - \phi_n\|_{l^\infty} \leq \varepsilon.$$

Algorithm 2.1 PCG-ATKM

Precompute the coefficients \widehat{U}_k .

Set the iteration counter $n = 0$ and the initial data ϕ_0 .

while *not converged* **do**

Step 1: Compute Φ_n via ATKM.

Step 2: $r_n = H_{\phi_n} \phi_n - \mu_{\phi_n} \phi_n$ with $\mu_{\phi_n} = \langle H_{\phi_n} \phi_n, \phi_n \rangle$.

Step 3: $p_n = \begin{cases} J_{\phi_n}(-Pr_n), & n = 0, \\ J_{\phi_n}(-Pr_n) + \beta_n^{cg} J_{\phi_n}(p_{n-1}), & \text{others.} \end{cases}$

Step 4: Correct the direction p_n and choose step size t_n :

- If $\langle H_{\phi_n} \phi_n, p_n \rangle < 0$, keep p_n unchanged; otherwise, set $p_n = J_{\phi_n}(-Pr_n)$.
- If $\langle H_{\phi_n} p_n, p_n \rangle + \langle g_n, p_n \rangle - \mu_{\phi_n} \|p_n\|^2 > 0$, take t_n as (2.24); otherwise, set $t_n = 0.3$.
- If $\mathcal{E}(\phi_{n+1}) \geq \mathcal{E}(\phi_n)$, decrease t_n by half until the energy decreases.

Step 5: $\phi_{n+1} = \cos(t_n \|p_n\|) \phi_n + \sin(t_n \|p_n\|) p_n / \|p_n\|$.

Step 6: $n = n + 1$.

end while

During each iteration, both the descent direction determination and step size approximation involve dipolar potentials evaluations. Given the spatial anisotropy exhibited by the wave function (density) in an anisotropic trap, the adoption of ATKM suits best the strong anisotropic setup in terms of memory requirement and computational cost. Using the same uniform mesh grid on the same domain, the combination of preconditioned conjugate gradient method and ATKM is quite natural and requires no additional efforts.

Direct solving the minimization problem (1.10) on a fixed fine mesh requires computations of high-dimensional functionals, therefore, it is quite time-consuming even though most of the computations can be accelerated by FFT, especially for 3D anisotropic system. The initial guesses are often inaccurate approximations of the ground state, which significantly postpones the convergence process, especially for cases that involve fast rotation and strong anisotropy. To alleviate such inefficiency, we adopt a cascading multigrid technique [6]. Numerical solution interpolated using coarser-mesh solution usually provides a better approximation than the commonly-used initial guesses, hence a faster convergence is expected and observed indeed in computation practice. Such cascading multigrid approach is summarized in **Algorithm 2.2**. Hereafter, we refer to it as PCG-ATKM-MG for convenience.

Algorithm 2.2 PCG-ATKM-MG

Given initial mesh grid \mathcal{T}^i with grid numbers $N_\alpha^i = k_\alpha \times 2^i$, $\alpha = x, y, z$.

Given an initial data ϕ_0^i on \mathcal{T}^i .

while not reach the finest mesh **do**

Step 1: Compute the ground state ϕ_g^i by utilizing **Algorithm 2.1**.

Step 2: Set ϕ_0^{i+1} by interpolating ϕ_g^i on the refined mesh \mathcal{T}^{i+1} .

Step 3: $i = i + 1$.

end while

REMARK 3. Under an isotropic trap, the algorithm PCG-KTM [6] serves as a suitable, accurate and efficient numerical method for computing the ground states of rotating dipolar BEC. While under an anisotropic trap, this method will require substantially large storage and more computational time, since the nonlocal potential solver KTM employs an isotropic truncation technique. As seen in [28], the total optimal zero-padding factor of KTM increases linearly with the anisotropy strength. This suggests that a prohibitively large memory requirement will be induced under an extremely strong anisotropic trap. Notably, the memory requirement of PCG-ATKM-MG is **independent** of the anisotropy strength.

REMARK 4. With appropriate modifications, the PCG-ATKM-MG can be extended to other related BEC models, such as multi-component BEC [37] and droplet dipolar BEC [33], which involves the famous Lee-Huang-Yang term [27] to describe the quantum fluctuation mechanism. We do not provide related details in this paper and shall leave them in some future work.

3. Numerical results. In this section, we test the accuracy and efficiency of PCG-ATKM-MG, and then apply it to study various vortices patterns, for example, bent vortices in rotating dipolar BEC. In addition, we investigate the impacts of model parameters on the critical rotational frequency, and study the variations of energies and chemical potential in details.

In the following experiments, we consider the harmonic potential (1.4), choose the rectangular domain $\mathcal{D}_{L\xi}$ and discretize it uniformly in each spatial direction. We take an equal number of grid points in each spatial direction, and the algorithm is executed with a three-level multigrid starting from $N/4^3$ total points to N points. As for the initial guesses, we have the following 10 choices [6]:

$$\begin{aligned}
(a) \phi_a(\mathbf{x}) &= \frac{1}{\sqrt[4]{\pi^3}} e^{-\frac{|\mathbf{x}|^2}{2}}, & (b) \phi_b(\mathbf{x}) &= \frac{(x+iy)\phi_a(\mathbf{x})}{\|(x+iy)\phi_a(\mathbf{x})\|_{L^2}}, & (\bar{b}) \phi_{\bar{b}}(\mathbf{x}) &= \bar{\phi}_b(\mathbf{x}), \\
(c) \phi_c(\mathbf{x}) &= \frac{\phi_a(\mathbf{x})+\phi_b(\mathbf{x})}{\|\phi_a(\mathbf{x})+\phi_b(\mathbf{x})\|_{L^2}}, & (\bar{c}) \phi_{\bar{c}}(\mathbf{x}) &= \bar{\phi}_c(\mathbf{x}), \\
(d) \phi_d(\mathbf{x}) &= \frac{(1-\Omega)\phi_a(\mathbf{x})+\Omega\phi_b(\mathbf{x})}{\|(1-\Omega)\phi_a(\mathbf{x})+\Omega\phi_b(\mathbf{x})\|_{L^2}}, & (\bar{d}) \phi_{\bar{d}}(\mathbf{x}) &= \bar{\phi}_d(\mathbf{x}), \\
(e) \phi_e(\mathbf{x}) &= \frac{\Omega\phi_a(\mathbf{x})+(1-\Omega)\phi_b(\mathbf{x})}{\|\Omega\phi_a(\mathbf{x})+(1-\Omega)\phi_b(\mathbf{x})\|_{L^2}}, & (\bar{e}) \phi_{\bar{e}}(\mathbf{x}) &= \bar{\phi}_e(\mathbf{x}), & (f) \phi_f(\mathbf{x}) &= \frac{\phi_g^{\text{TF}}(\mathbf{x})}{\|\phi_g^{\text{TF}}(\mathbf{x})\|_{L^2}},
\end{aligned}$$

where

$$\phi_g^{\text{TF}}(\mathbf{x}) = \begin{cases} \sqrt{(\mu_g^{\text{TF}} - V(\mathbf{x}))/\beta}, & V(\mathbf{x}) < \mu_g^{\text{TF}}, \\ 0, & \text{otherwise,} \end{cases} \quad \text{with} \quad \mu_g^{\text{TF}} = \frac{1}{2} \left(\frac{15\beta\gamma_x\gamma_y\gamma_z}{4\pi} \right)^{2/5}.$$

In practice, we choose the stopping criterion (2.25) with $\varepsilon = 10^{-10}$ unless stated otherwise, and select numerical solution with the lowest energy as the ground state, which is denoted as ϕ_g^{h} hereafter. When the trap is chosen as the harmonic potential

(1.4), the energies associated with stationary state ϕ (1.9) satisfy the following **virial identity** [8]

$$(3.1) \quad 0 = I(\phi) := 2E_{\text{kin}}(\phi) - 2E_{\text{pot}}(\phi) + 3E_{\text{int}}(\phi) + 3E_{\text{dip}}(\phi),$$

with

$$E_{\text{kin}}(\phi) = \int_{\mathbb{R}^3} \frac{1}{2} |\nabla \phi|^2 d\mathbf{x}, \quad E_{\text{pot}}(\phi) = \int_{\mathbb{R}^3} V(\mathbf{x}) |\phi|^2 d\mathbf{x},$$

$$E_{\text{int}}(\phi) = \int_{\mathbb{R}^3} \frac{\beta}{2} |\phi|^4 d\mathbf{x}, \quad E_{\text{dip}}(\phi) = \int_{\mathbb{R}^3} \frac{\lambda}{2} \Phi |\phi|^2 d\mathbf{x}.$$

The numerical approximation of the above virial identity (3.1) is denoted as $I^{\mathbf{h}}$, and we adopt its absolute value $|I^{\mathbf{h}}|$ as the virial-identity residual so as to measure its approximation accuracy. The algorithm is implemented in Fortran, and all reported timing results are obtained using a Intel(R) Xeon(R) Gold6248R CPU 3.00GHz with 36 MB cache with the Intel ifort and optimization level -O3 in Ubuntu GNU/Linux.

3.1. Accuracy confirmation and efficiency performance. In this subsection, we shall present the spectral spatial accuracy and efficiency performance of our method for both isotropic and anisotropic traps with different physical parameters.

Note that the equality $E(\phi) = E(\kappa\phi)$ holds for any $\kappa \in \mathbb{C}$ with $|\kappa| = 1$. Consequently, the numerical errors are measured in relative l^2 -norm as follows

$$E_2 := \|\phi_g^{\mathbf{h}} - \kappa \phi_g\|_{\mathbf{h}} / \|\phi_g\|_{\mathbf{h}}, \quad \kappa = \langle \phi_g^{\mathbf{h}}, \phi_g \rangle_{\mathbf{h}} / \langle \phi_g, \phi_g \rangle_{\mathbf{h}},$$

where $\langle f, g \rangle_{\mathbf{h}} := h_x h_y h_z \sum_{\mathbf{j} \in \mathcal{I}_{\mathbf{N}}} f_{\mathbf{j}} \bar{g}_{\mathbf{j}}$ is the inner product of two complex-valued grid functions, the ‘exact’ ground state ϕ_g is obtained numerically on a very fine mesh ($N = 512^3$), and $\phi_g^{\mathbf{h}}$ is the numerical solution computed with mesh size \mathbf{h} .

It is worthy to point out that, the energy is rotational invariant under isotropic traps, that is, $E(\phi(R_\alpha \mathbf{x})) = E(\kappa \phi(\mathbf{x}))$ holds for any rotational matrix

$$R_\alpha = \begin{pmatrix} \cos \alpha & -\sin \alpha \\ \sin \alpha & \cos \alpha \end{pmatrix}, \quad \forall \alpha \in [0, 2\pi].$$

As the rotational frequency increases beyond the critical value, the ground state develops more than one vortex. In such cases, it is inappropriate to use E_2 to measure the numerical approximation errors. Thus we introduce a modified error defined as

$$\widetilde{E}_2 := \min_{\alpha} \|\phi_g^{\mathbf{h}}(R_\alpha \mathbf{x}) - \kappa_\alpha \phi_g(\mathbf{x})\|_{\mathbf{h}} / \|\phi_g(\mathbf{x})\|_{\mathbf{h}}, \quad \kappa_\alpha = \langle \phi_g^{\mathbf{h}}(R_\alpha \mathbf{x}), \phi_g(\mathbf{x}) \rangle_{\mathbf{h}} / \langle \phi_g(\mathbf{x}), \phi_g(\mathbf{x}) \rangle_{\mathbf{h}}.$$

The above optimization problem is solved using the interior-point method [30], which has been implemented in the built-in function ‘fmincon’ of Matlab. The function-rotation mapping, from $\phi(\mathbf{x})$ to $\phi(R_\alpha \mathbf{x})$, is implemented efficiently and accurately with FFT via the fast-rotation algorithm based on shear-decomposition [29, 40].

EXAMPLE 3.1. (Accuracy and efficiency tests) Given dipole orientation $\mathbf{n} = (0, 0, 1)^T$, $\beta = 100$ and $\lambda = 0.8\beta$, we compute the ground states for different rotational frequencies Ω in the following two cases:

Case I (Isotropic trap): $\gamma_x = \gamma_y = \gamma_z = 1$;

Case II (Anisotropic trap): $\gamma_x = 1, \gamma_y = 2, \gamma_z = 10$.

We set the stopping criterion (2.25) as $\varepsilon = 10^{-12}$, and choose domain $\mathcal{D}_{L\xi} = [-16, 16]^3$ for **Case I** and $\mathcal{D}_{L\xi} = [-16, 16]^2 \times [-10, 10]$ for **Case II** due to its anisotropic trap.

Table 1 shows the relative l^2 errors E_2 , \widetilde{E}_2 and the virial-identity residual $|I^h|$ for **Case I-II**, and Fig. 1 presents the contour plots of ‘exact’ ground state $|\phi_g(x, y, z = 0)|^2$ and numerical ground state $|\phi_g^h(x, y, z = 0)|^2$ with $N = 256^3$ for $\Omega = 0.85$ in **Case I**. We can observe that errors E_2 , \widetilde{E}_2 and $|I^h|$ converge spectrally accurate with respect to the spatial mesh size for all cases. Fig. 2 displays the computational time (measured in seconds), from which we know that the efficiency exhibits a typical complexity of $\mathcal{O}(N \log N)$ similar as FFT. This behavior agrees well with our expectation because the number of iterations in each computation is significantly smaller than the grid number N . To sum up, PCG-ATKM-MG is an accurate and efficient numerical solver for computing ground states in both isotropic and anisotropic cases.

Table 1: Numerical errors for both isotropic and anisotropic traps in **Example 3.1**.

Case I: $\gamma_x = \gamma_y = \gamma_z = 1$					
Ω	N	32^3	64^3	128^3	256^3
0.2	E_2	4.1267E-03	2.3477E-05	2.1482E-09	2.2755E-12
	$ I^h $	2.1743E-02	2.5129E-05	1.6822E-11	1.3450E-12
0.4	E_2	4.2588E-03	2.3483E-05	2.1482E-09	4.3439E-12
	$ I^h $	2.1810E-02	2.5129E-05	1.5696E-11	2.0317E-13
0.6	E_2	4.6460E-03	2.3493E-05	2.1482E-09	6.9024E-12
	$ I^h $	2.1959E-02	2.5129E-05	1.5724E-11	4.8439E-13
0.8 (1 vortex)	E_2	1.0000	8.5676E-05	4.9185E-09	3.7105E-11
	$ I^h $	9.3167E-02	1.2527E-04	2.7377E-11	1.1491E-13
0.85 (2 vortices)	\widetilde{E}_2	1.1340E-01	7.9153E-04	1.4546E-07	3.4234E-09
	$ I^h $	1.0275E-01	5.6180E-05	4.3209E-11	6.9289E-12
Case II: $\gamma_x = 1, \gamma_y = 2, \gamma_z = 10$					
Ω	N	32^3	64^3	128^3	256^3
0.2	E_2	1.0737E-01	2.5143E-03	2.4725E-06	1.0235E-11
	$ I^h $	4.3461	5.4160E-02	3.7568E-06	4.4853E-12
0.4	E_2	1.1212E-01	2.5217E-03	2.4340E-06	3.3305E-11
	$ I^h $	4.4398	5.5158E-02	3.5739E-06	2.2435E-12
0.6	E_2	3.1052E-01	2.5985E-03	2.3537E-06	9.1651E-11
	$ I^h $	4.6578	5.6558E-02	2.9120E-06	3.7419E-12
0.8 (2 vortices)	E_2	7.8085E-01	4.7745E-02	8.7262E-06	3.5937E-10
	$ I^h $	4.5065	2.8864E-02	5.6266E-06	1.1440E-11

3.2. Bent vortices in dipolar BEC. Bent vortices are known to emerge in elongated rotating BEC with strong local interactions, and their behavior in the absence of dipolar potential has been well established in previous studies [2, 21, 22]. Building on this foundation, this subsection investigates bent vortices in the presence

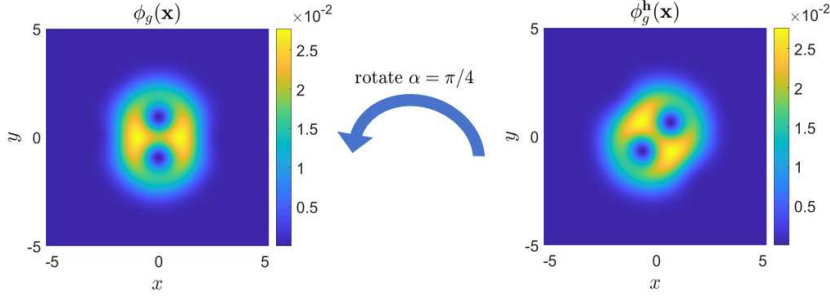


Fig. 1: Contour plots of $|\phi_g(x, y, z = 0)|^2$ and $|\phi_g^h(x, y, z = 0)|^2$ with $N = 256^3$ for $\Omega = 0.85$ of **Case I** in **Example 3.1**.

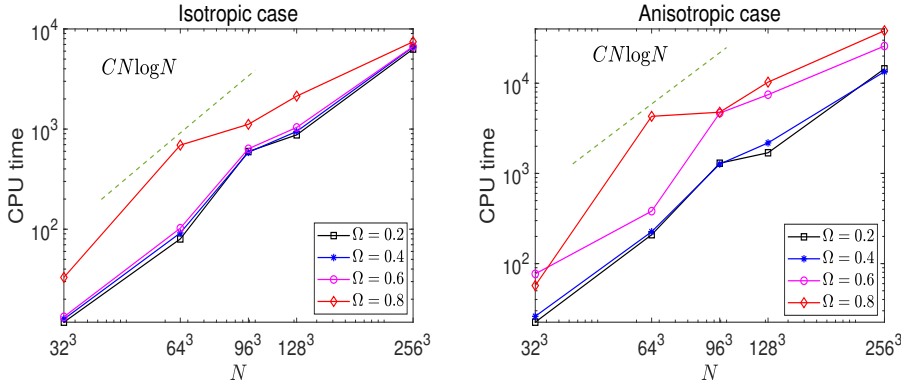


Fig. 2: Computational time for **Case I** (left) and **Case II** (right) in **Example 3.1**.

of dipolar potential. Hereafter, if not explicitly stated, we shall mix ϕ_g^h and ϕ_g just for presentation simplicity.

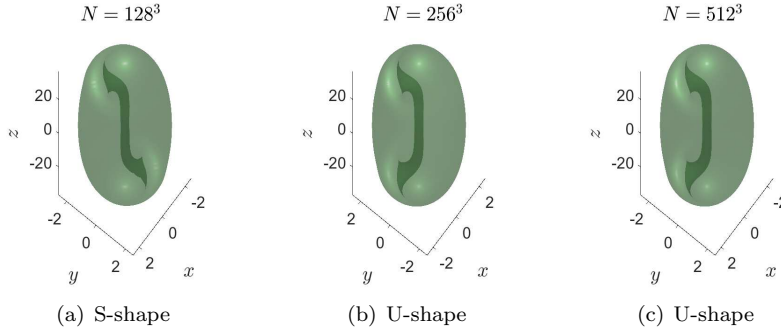
EXAMPLE 3.2. (*U-shape vortex line*) Given $\gamma_x = \gamma_y = 1$, $\gamma_z = 0.05$, $\beta = 1000$, $\lambda = -300$, $\mathbf{n} = (0, 0, 1)^T$ and $\Omega = 0.75$, we choose domain $\mathcal{D}_{L\xi} = [-10, 10]^2 \times [-100, 100]$ and take grid numbers $N = 128^3, 256^3, 512^3$ respectively to compute the ground state.

Table 2 presents the energies E , virial-identity residual $|I^h|$ and Hamiltonian residual $\|r_n\|$ for different N , and Fig. 3 shows the corresponding isosurface plots of $|\phi_g(\mathbf{x})|^2 = 3 \times 10^{-4}$. These results indicate that the U-shape vortex state is more likely to be the ground state. Conversely, the S-shape vortex state calculated with $N = 128^3$ is not the ground state, since its associated virial-identity residual $|I^h|$ is relatively large with only 5-digit accuracy (9.0018×10^{-6} as shown in Table 2) due to the insufficient grid number. The vortex structure is quite subtle and its computation is sensitive to the mesh size, therefore, the mesh should be chosen as fine as possible, which of course poses a great numerical challenge especially for anisotropic trap and strong dipolar potential cases.

EXAMPLE 3.3. (*Bent vortices under different dipolar potentials*) Given $\gamma_x = \gamma_y = 1$, $\gamma_z = 0.1$ and $\beta = 9000$, we compute the ground states for both $\Omega = 0.41$

Table 2: Energies E , $|I^h|$ and $\|r_n\|$ for different N in **Example 3.2**.

N	E	$ I^h $	$\ r_n\ $
128^3	2.276210347750	9.0018E-06	5.1475E-09
256^3	2.276210390179	2.8555E-11	7.8405E-09
512^3	2.276210390179	3.0787E-12	7.4651E-09

Fig. 3: Isosurface plots of $|\phi_g(\mathbf{x})|^2 = 3 \times 10^{-4}$ with different N in **Example 3.2**.

and $\Omega = 0.49$ in following cases:

Case I: $\lambda = 0$;

Case II: $\lambda = 4000$, $\mathbf{n} = (0, 0, 1)^T$;

Case III: $\lambda = 4000$, $\mathbf{n} = (1, 0, 0)^T$;

Case IV: $\lambda = -4000$, $\mathbf{n} = (0, 0, 1)^T$.

The computation is done on $\mathcal{D}_{L\xi} = [-10, 10]^2 \times [-100, 100]$ with $N = 384^3$. Fig. 4 shows the isosurfaces of the densities $|\phi_g(\mathbf{x})|^2$, from which we conclude that the dipolar potential affects vortex patterns, including number of vortices and length of the central vortex line. In addition, for $\mathbf{n} = (0, 0, 1)^T$, there are more vortices in the ground state for negative λ than its positive counterpart (cf. the second and fourth columns of Fig. 4).

3.3. Critical rotational frequency. In rotating BEC, a vortex appears in the ground state only if the rotational frequency Ω exceeds certain critical value Ω_c . In this subsection, we shall investigate how the critical rotational frequency Ω_c varies with trapping frequencies of the harmonic potential (1.4), local interaction strength β , dipolar potential strength λ and the dipole orientation \mathbf{n} , respectively. Unless stated otherwise, we take $\mathcal{D}_{L\xi} = [-10, 10]^3$ and $N = 128^3$.

EXAMPLE 3.4. (The impacts of external potential and local interaction) In the absence of dipolar potential, i.e., $\lambda = 0$, we investigate the variations of Ω_c in the following cases:

Case I: Let $\beta = 2000$, $\gamma_x = \gamma_z = 1$ and vary γ_y ;

Case II: Let $\beta = 2000$, $\gamma_x = \gamma_y = 1$ and vary γ_z ;

Case III: Let $\gamma_x = \gamma_y = \gamma_z = 1$ and vary β .

For **Case I-II**, the computation domain is chosen as $\mathcal{D}_{L\xi} = [-16, 16]^3$ with grid number $N = 256^3$. Fig. 5 depicts the variations of critical rotational frequency

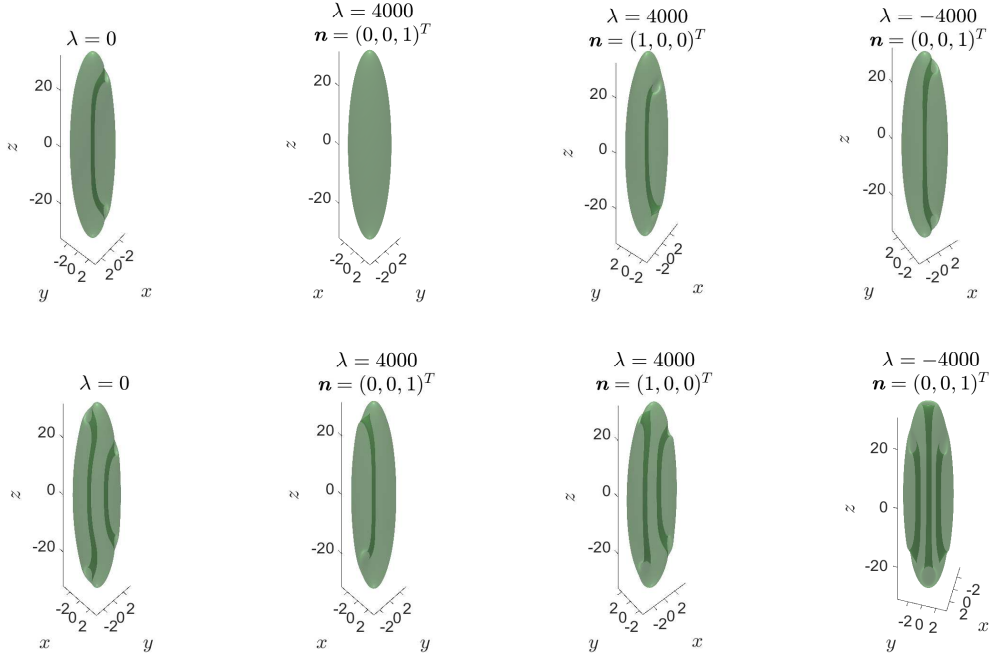


Fig. 4: Isosurfaces of $|\phi_g(\mathbf{x})|^2 = 3 \times 10^{-4}$ for $\Omega = 0.41$ (top row) and $\Omega = 0.49$ (bottom row) in **Case I-IV** (from left to right) of **Example 3.3**.

Ω_c with respect to the trapping frequencies γ_y , γ_z and local interaction strength β respectively. From this figure, we can observe clearly that: (i) The critical rotational frequency Ω_c increases with γ_y , in contrast to its decreasing trend with γ_z . (ii) The critical rotational frequency Ω_c decreases as β increases, and it decreases faster for smaller β . Moreover, based on extensive numerical results not shown here, it is reasonable to conjecture that Ω_c tends to one when β tends to zero.

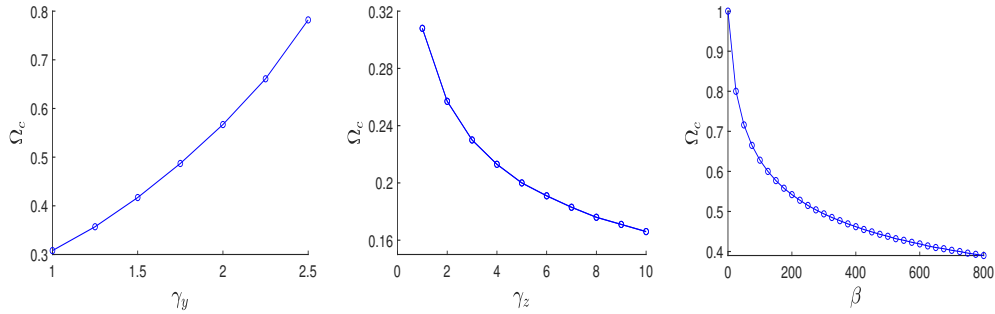


Fig. 5: The variations of Ω_c for **Case I-III** in **Example 3.4**.

EXAMPLE 3.5. (The impact of dipolar potential) Given an isotropic harmonic potential, i.e., $V(\mathbf{x}) = \frac{1}{2}|\mathbf{x}|^2$, we investigate the variations of Ω_c in the following cases:

Case I: Let $\mathbf{n} = (0, 0, 1)^T$, take $\beta = 200, 300, 400$ and vary λ ;

Case II: Same as **Case I** except for $\mathbf{n} = (1, 0, 0)^T$;

Case III: Let $\beta = 400$, $\mathbf{n} = (\sin \theta, 0, \cos \theta)^T$ with varying $\theta \in [0, \pi]$, and take $\lambda = 0, \pm 50, \pm 100, \pm 200$ respectively.

Fig. 6 depicts the variations of critical rotational frequency Ω_c with respect to the dipolar potential strength λ in **Case I-II** and the angle θ in **Case III**. From this figure, it is clear that Ω_c increases as λ increases when the dipole orientation $\mathbf{n} = (0, 0, 1)^T$. For orientation $\mathbf{n} = (1, 0, 0)^T$, Ω_c increases as $|\lambda|$ increases when $\lambda < 0$. While, for positive λ , it first decreases and then increases as λ increases. From the numerical results not shown here for brevity, given an isotropic harmonic potential $V(\mathbf{x})$, we conclude that: (i) When the dipole orientation \mathbf{n} lies in the x - y plane, the variation behavior of Ω_c is the same as that of the case $\mathbf{n} = (1, 0, 0)^T$. (ii) There is no dependence of Ω_c on the azimuthal angle of the orientation \mathbf{n} .

In the third picture of Fig. 6, θ denotes the angle between the dipole orientation \mathbf{n} and the rotation axis (z -axis). For positive λ , Ω_c decreases as the dipole orientation rotates from parallel ($\theta = 0, \pi$) to perpendicular ($\theta = \pi/2$) alignment relative to the rotation axis, while for negative λ , it increases. Moreover, the magnitude of this variation in Ω_c is smaller for a given positive $\lambda = \alpha$ than for its negative counterpart $\lambda = -\alpha$.

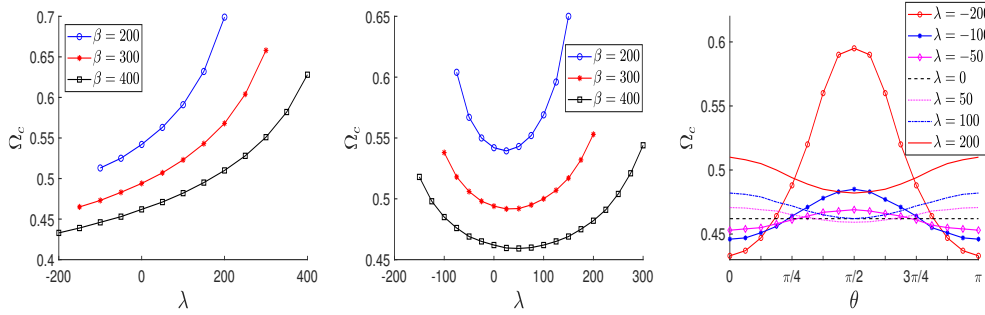


Fig. 6: The variations of Ω_c with λ for $\mathbf{n} = (0, 0, 1)^T$, $(1, 0, 0)^T$ and that with θ in $\mathbf{n} = (\sin \theta, 0, \cos \theta)^T$ (from left to right) of **Example 3.5**.

3.4. Impacts on energies and chemical potential. In this subsection, we study the variation trends of chemical potential μ and energies E , E_{kin} , E_{pot} , E_{int} , E_{dip} , $E_{\text{rot}} := -\Omega \int_{\mathbb{R}^3} \bar{\psi} L_z \psi d\mathbf{x}$ with respect to different physical parameters, including trapping frequencies of the harmonic potential (1.4), local interaction strength β , dipolar potential strength λ and rotational frequency Ω . We choose computation domain $\mathcal{D}_{L\xi} = [-20, 20]^3$ and take grid number $N = 256^3$, if not stated otherwise.

EXAMPLE 3.6. (The impact of external potential) Here, we investigate the dependence of the energies and chemical potential on the external potential. To this end, we choose the harmonic potential with $\gamma_y = 1$, $\beta = 600$, $\Omega = 0.6$, $\lambda = -200$, $\mathbf{n} = (0, 0, 1)^T$ and consider the following cases:

Case I: Let $\gamma_z = 1$ and vary γ_x ;

Case II: Let $\gamma_x = 1$ and vary γ_z .

Fig. 7 depicts the variations of energies and chemical potential in **Case I-II**, from which we can see that: (i) Only the energies E and E_{dip} vary continuously, whereas

chemical potential μ and $E_{\text{kin}}, E_{\text{pot}}, E_{\text{int}}, E_{\text{rot}}$ exhibit ‘jumps’ at the phase transition point where the vortex number changes. (ii) The energy E exhibits a monotonic increase with respect to both γ_x and γ_z . (iii) The energy E_{dip} exhibits a monotonic increase (decrease) with respect to γ_x (γ_z).

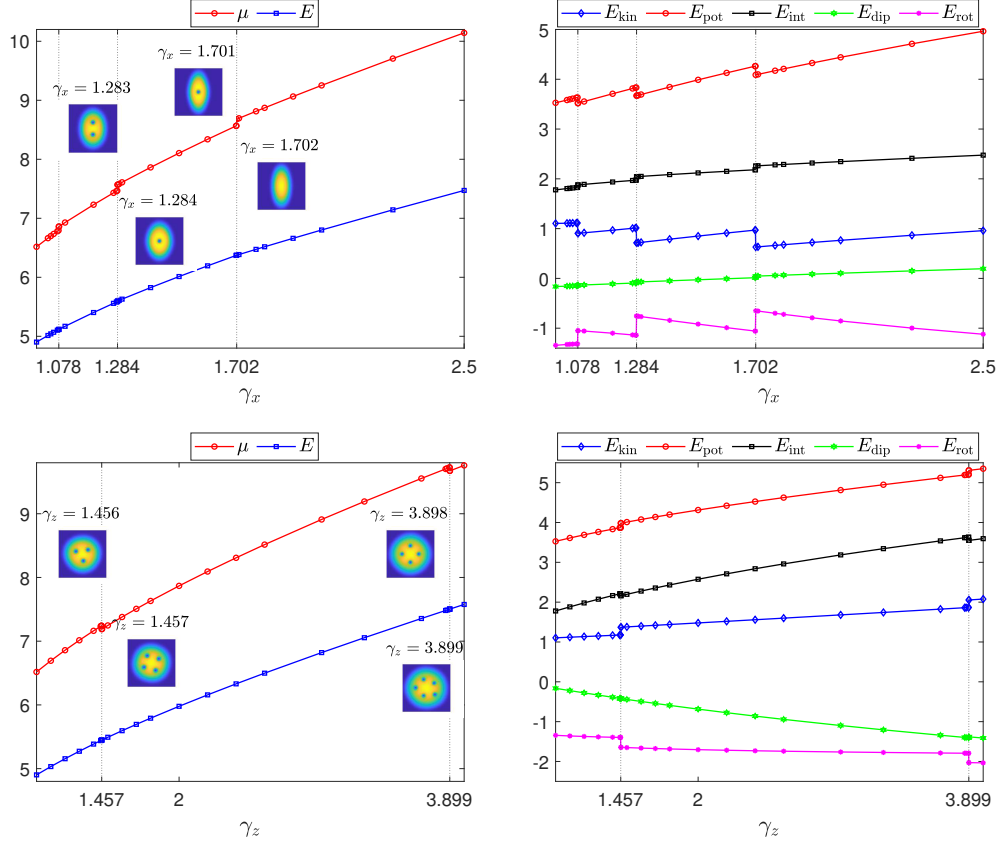


Fig. 7: The variations of energies and μ for **Case I-II** (from top to bottom) in **Example 3.6**.

EXAMPLE 3.7. (The impacts of short/long-range interaction and rotational frequency) Given the dipole orientation $\mathbf{n} = (0, 0, 1)^T$ and an isotropic harmonic potential, i.e., $V(\mathbf{x}) = \frac{1}{2}|\mathbf{x}|^2$, we investigate the variations of energies and chemical potential in the following cases:

Case I: Let $\Omega = 0.6$, $\lambda = -200$, and vary β ;

Case II: Let $\Omega = 0.6$, $\beta = 600$, and vary λ ;

Case III: Let $\beta = 600$, $\lambda = -200$, and vary Ω .

We take computation domain $\mathcal{D}_{L\xi} = [-16, 16]^3$ for all cases. Fig. 8 depicts the variations of energies and chemical potential, from which we can see clearly that: (i) Only the energies E and E_{dip} vary continuously, whereas chemical potential μ and $E_{\text{kin}}, E_{\text{pot}}, E_{\text{int}}, E_{\text{rot}}$ display abrupt discontinuities in the presence of phase transition in the ground state. (ii) Both E and E_{dip} increase (decrease) monotonically with respect to β (Ω). (iii) Under an isotropic trap, when there is no vortex in the ground

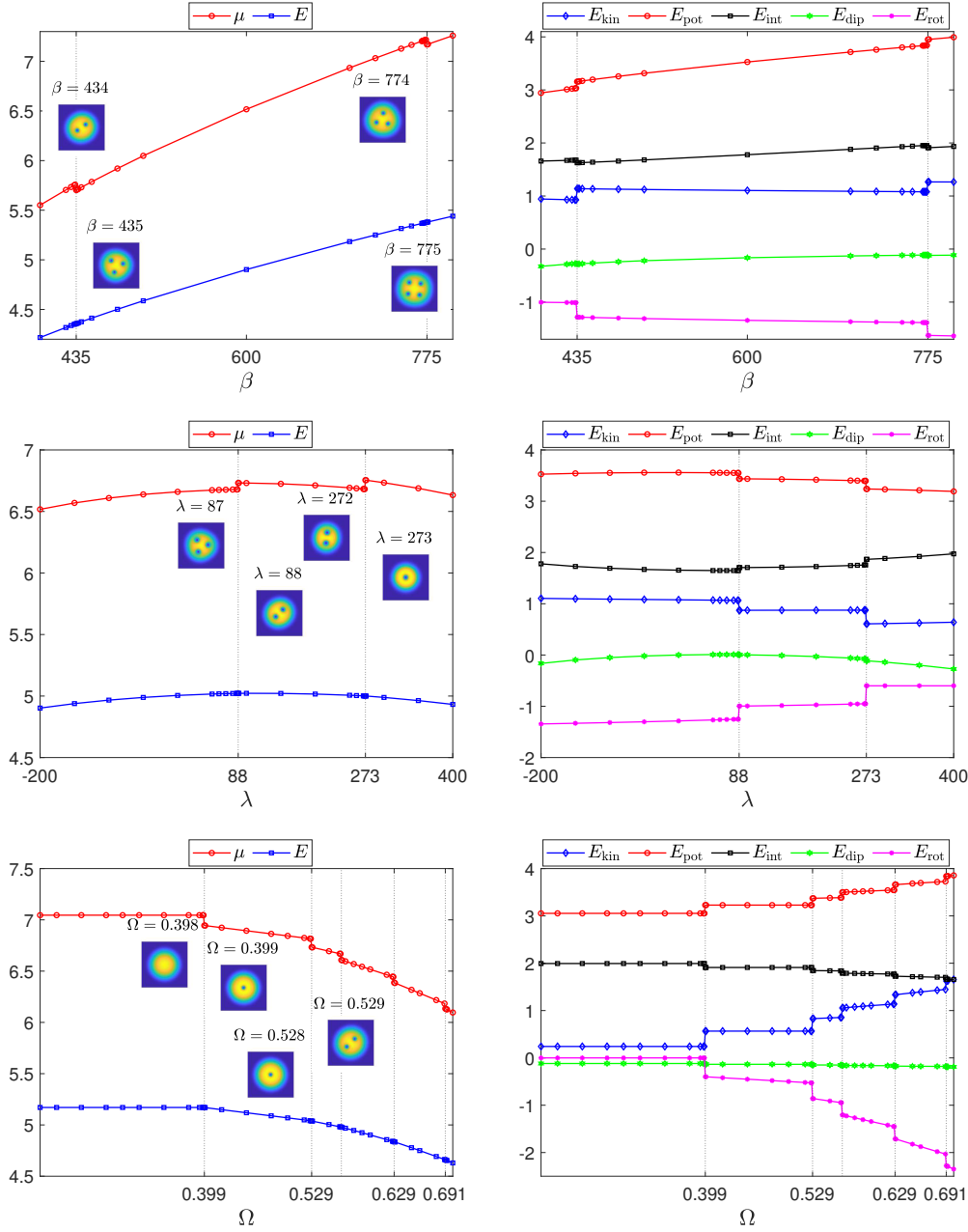


Fig. 8: The variations of energies and μ for **Case I-III** (from top to bottom) in **Example 3.7**.

state, all the energies and chemical potential μ remain unchanged as Ω increases.

3.5. Patterns of ground states in anisotropic traps. Here we compute the ground states of anisotropic rotating dipolar BEC and present the corresponding ground state patterns. In the following numerical tests, we take $\beta = 5000$, $\Omega = 0.85$,

$\gamma_y = \gamma_z = 1$ and choose computation domain $\mathcal{D}_{L\xi} = [-14, 14]^3$ with grid number $N = 256^3$.

EXAMPLE 3.8. (Non-dipolar BEC) *In the absence of dipolar potential, i.e., $\lambda = 0$, we take $\gamma_x = 1, 1.5, 2, 3$ respectively and compute the ground states.*

Fig. 9 depicts the contour plots of $|\phi_g(x, y, z = 0)|^2$ and corresponding isosurface plots of $|\phi_g(\mathbf{x})|^2 = 3 \times 10^{-4}$ for different γ_x , from which we can see that: (i) The vortex lines are parallel to the rotation axis. (ii) Under an isotropic harmonic potential, the vortex lattice exhibits a triangular arrangement characteristic of the Abrikosov lattice (cf. the first column in Fig. 9). (iii) As γ_x increases, i.e., the anisotropy strength becomes stronger, the density profile gradually narrows in the x -direction and the number of vortices decreases.

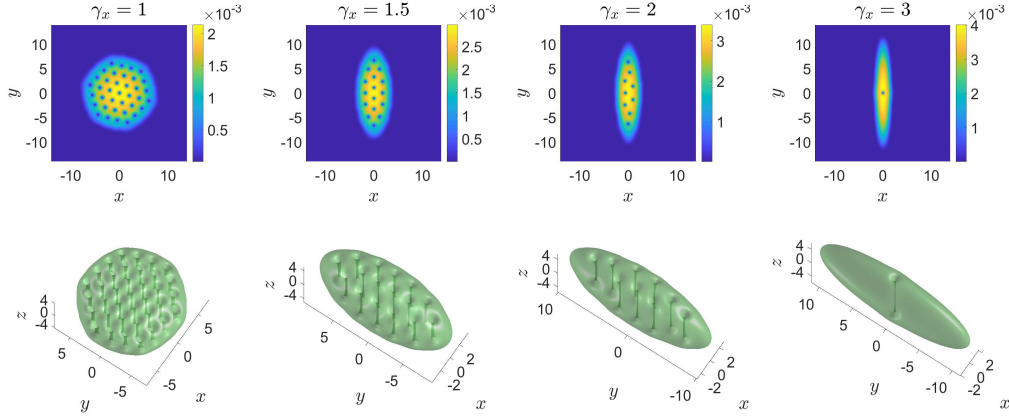


Fig. 9: Contour plots of $|\phi_g(x, y, z = 0)|^2$ (top row) and isosurface plots of $|\phi_g(\mathbf{x})|^2 = 3 \times 10^{-4}$ (bottom row) in **Example 3.8**.

EXAMPLE 3.9. (Dipolar BEC) *Taking $\gamma_x = 1, 1.5, 2, 3$ respectively, we compute the ground states in the following cases:*

Case I: Let $\lambda = -2000$ and different dipole orientations:

$$(a) \mathbf{n} = (1, 0, 0)^T; \quad (b) \mathbf{n} = (0, 0, 1)^T;$$

Case II: Let $\lambda = 2000$ and different dipole orientations:

$$(c) \mathbf{n} = (1, 0, 0)^T; \quad (d) \mathbf{n} = (1/2, 1/2, \sqrt{2}/2)^T.$$

Fig. 10 shows the contour plots of $|\phi_g(x, y, z = 0)|^2$ for all cases respectively. Clearly, the dipole orientation significantly influences the ground state patterns. The arrangement of the vortices mainly depends on \mathbf{n}_\perp , the x - y plane component of the dipole orientation \mathbf{n} . When $\lambda < 0$, the vortices tend to align along the direction that is perpendicular to \mathbf{n}_\perp (**Case I**); when $\lambda > 0$, the vortices tend to align along with \mathbf{n}_\perp (**Case II**). As for $\mathbf{n} = (0, 0, 1)^T$, the distribution of vortices is similar to that in the case of non-dipolar BEC (cf. Fig. 9), but more vortices are induced with $\lambda < 0$.

4. Conclusion. We proposed an accurate and efficient numerical method to compute the ground states of 3D rotating dipolar Bose-Einstein condensates under strongly anisotropic traps. To address challenges posed by the fast rotation and strongly anisotropic traps, we incorporate the anisotropic truncated kernel method (ATKM) for dipolar potential evaluation into the preconditioned conjugate gradient method (PCG). The proposed method is spectrally accurate and efficient, and its

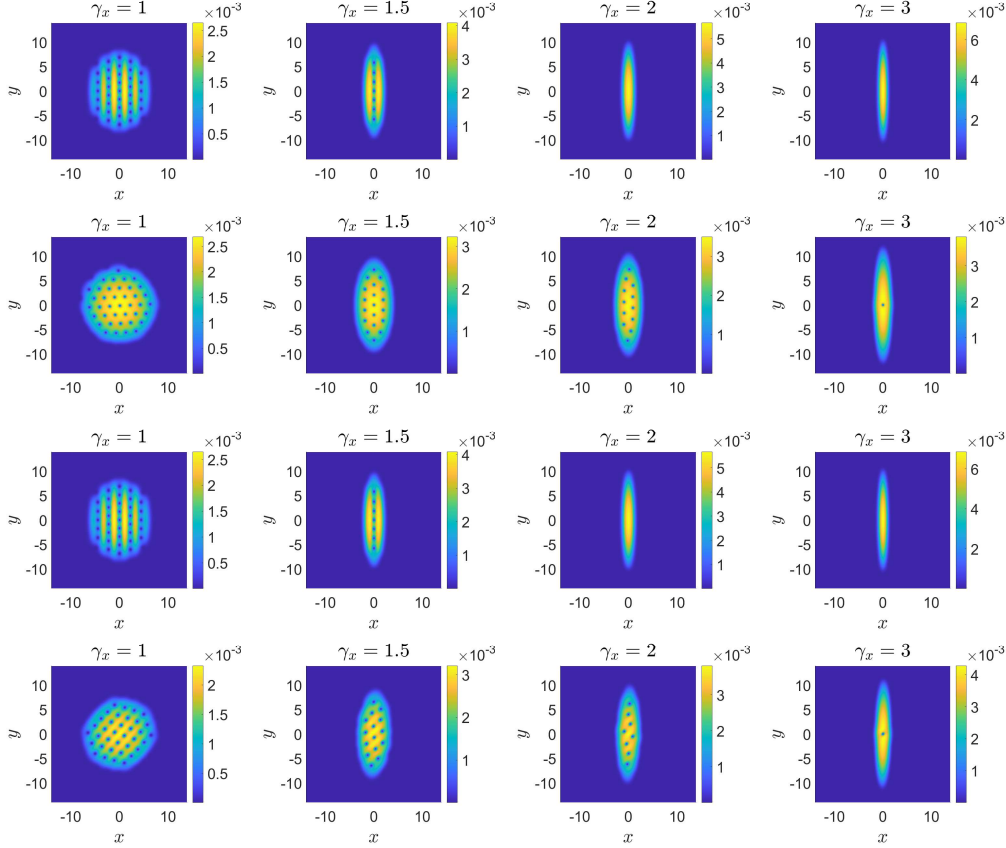


Fig. 10: Contour plots of $|\phi_g(x, y, z = 0)|^2$ for **Case I** (top two rows) and **Case II** (bottom two rows) in **Example 3.9**.

memory requirement is independent of the anisotropy strength. We presented extensive numerical results to confirm the accuracy and efficiency, together with applications to the impacts of different model parameters on critical rotational frequency, energies and chemical potential. In addition, we observed bent vortices (U-shape) in dipolar BEC and carried out a careful and comprehensive numerical computation. Novel ground state patterns were identified numerically, and the influences of anisotropy strength and dipolar potential on the number and arrangement of vortices were investigated. Our method can be extended to more general systems, such as multi-component and droplet dipolar BEC, with appropriate modifications and we shall report them in future work.

REFERENCES

- [1] P.-A. ABSIL, R. MAHONY AND R. SEPULCHRE, *Optimization Algorithms on Matrix Manifolds*, Princeton University Press, 2008.
- [2] A. AFTALION AND I. DANAILA, *Three-dimensional vortex configurations in a rotating Bose-Einstein condensate*, Phys. Rev. A, **68** (2003), article 023603.
- [3] R. ALTMANN, P. HENNING AND D. PETERSEIM, *The J-method for the Gross-Pitaevskii*

- eigenvalue problem*, Numer. Math., **148** (2021), 575–610.
- [4] M. H. ANDERSON, J. R. ENSHER, M. R. MATTHEWA, C. E. WIEMAN AND E. A. CORNELL, *Observation of Bose-Einstein condensation in a dilute atomic vapor*, Science, **269** (1995), 198–201.
- [5] X. ANTOINE, A. LEVITT AND Q. TANG, *Efficient spectral computation of the stationary states of rotating Bose-Einstein condensates by preconditioned nonlinear conjugate gradient methods*, J. Comput. Phys., **343** (2017), 92–109.
- [6] X. ANTOINE, Q. TANG AND Y. ZHANG, *A preconditioned conjugated gradient method for computing ground states of rotating dipolar Bose-Einstein condensates via kernel truncation method for dipole-dipole interaction evaluation*, Commun. Comput. Phys., **24**(4) (2018), 966–988.
- [7] W. BAO, N. B. ABDALLAH AND Y. CAI, *Gross-Pitaevskii-Poisson equations for dipolar Bose-Einstein condensate with anisotropic confinement*, SIAM J. Math. Anal., **44** (2012), 1713–1741.
- [8] W. BAO AND Y. CAI, *Mathematical theory and numerical methods for Bose-Einstein condensation*, Kinet. Relat. Models, **6** (2013), 1–135.
- [9] W. BAO, Y. CAI AND H. WANG, *Efficient numerical methods for computing ground states and dynamics of dipolar Bose-Einstein condensates*, J. Comput. Phys., **229** (2010), 7874–7892.
- [10] W. BAO AND Q. DU, *Computing the ground state solution of Bose-Einstein condensates by a normalized gradient flow*, SIAM J. Sci. Comput., **25** (2004), 1674–1697.
- [11] W. BAO, H. JIAN, N. J. MAUSER AND Y. ZHANG, *Dimension reduction of the Schrödinger equation with Coulomb and anisotropic confining potentials*, SIAM J. Appl. Math., **73** (6) (2013), 2100–2123.
- [12] W. BAO, S. JIANG, Q. TANG AND Y. ZHANG, *Computing the ground state and dynamics of the nonlinear Schrödinger equation with nonlocal interactions via the nonuniform FFT*, J. Comput. Phys., **296** (2015), 72–89.
- [13] M. A. BARANOV, *Theoretical progress in many body physics of dipolar gases*, Phys. Rep., **464** (2008), 71–111.
- [14] N. BIGAGLI, W. YUAN, S. ZHANG, B. BULATOVIC, T. KARMAN, I. STEVENSON AND S. WILL, *Observation of Bose-Einstein condensation of dipolar molecules*, Nature, **631** (2024), 289–293.
- [15] N. BOUMAL, *An introduction to optimization on smooth manifolds*, Cambridge University Press, 2023.
- [16] C. C. BRADLEY, C. A. SACKETT, J. J. TOLLETT AND R. G. HULET, *Evidence of Bose-Einstein condensation in an atomic gas with attractive interactions*, Phys. Rev. Lett., **75** (1995), 1687–1690.
- [17] E. CASOTTI, E. POLI, L. KLAUS, A. LITVINOV, C. ULM, C. POLITI, M. J. MARK, T. BLAND AND F. FERLAINO, *Observation of vortices in a dipolar supersolid*, Nature, **635** (2024), 327–331.
- [18] K. B. DAVIS, M. O. MEWES, M. R. ANDREWS, N. J. VAN DRUTEN, D. S. DURFEE, D. M. KURN AND W. KETTERLE, *Bose-Einstein condensation in a gas of sodium atoms*, Phys. Rev. Lett., **75** (1995), 3969–3973.
- [19] C. M. DION AND E. CANCES, *Ground state of the time-independent Gross-Pitaevskii equation*, Comput. Phys. Commun., **177** (2007), 787–798.
- [20] L. EXL, N. J. MAUSER AND Y. ZHANG, *Accurate and efficient computation of nonlocal potentials based on Gaussian-sum approximation*, J. Comput. Phys., **327** (2016), 629–642.
- [21] J. J. GARCÍA-RIPOLL AND V. M. PÉREZ-GARCÍA, *Vortex bending and tightly packed vortex lattices in Bose-Einstein condensates*, Phys. Rev. A, **64** (2001), article 053611.
- [22] J. J. GARCÍA-RIPOLL AND V. M. PÉREZ-GARCÍA, *Vortex nucleation and hysteresis phenomena in rotating Bose-Einstein condensates*, Phys. Rev. A, **63** (2001), article 041603(R).
- [23] A. L. GAUNT, T. F. SCHMIDT, I. GOTLIBOVYCH, R. P. SMITH AND Z. HADZIBABIC, *Bose-Einstein condensation of atoms in a uniform potential*, Phys. Rev. Lett., **110** (2013), article 200406.
- [24] L. GREENGARD, S. JIANG AND Y. ZHANG, *The anisotropic truncated kernel method for convolution with free-space Green’s functions*, SIAM J. Sci. Comput., **40** (2018), A3733–A3754.
- [25] L. JIA, A. WANG AND S. YI, *Low-lying excitations of vortex lattices in condensates with anisotropic dipole-dipole interaction*, Phys. Rev. A, **97** (2018), article 043614.

- [26] S. JIANG, L. GREENGARD AND W. BAO, *Fast and accurate evaluation of nonlocal Coulomb and dipole-dipole interactions via the nonuniform FFT*, SIAM J. Sci. Comput., **36** (2014), B777–B794.
- [27] T. LEE, K. HUANG AND C. YANG, *Eigenvalues and eigenfunctions of a Bose system of hard spheres and its low-temperature properties*, Phys. Rev., **106** (1957), 1135–1145.
- [28] X. LIU, Q. TANG, S. ZHANG AND Y. ZHANG, *On optimal zero-padding of kernel truncation method*, SIAM J. Sci. Comput., **46** (2024), A23–A49.
- [29] X. LIU, Y. YUAN AND Y. ZHANG, *An efficient compact splitting Fourier spectral method for computing the dynamics of rotating spin-orbit coupled spin-1 Bose-Einstein condensates*, J. Comput. Phys., **529** (2025), article 113892.
- [30] J. NOCEDAL AND S. J. WRIGHT, *Numerical Optimization*, Springer, 2006.
- [31] M. Ö. OKTEL, *Vortex lattice of a Bose-Einstein Condensate in a rotating anisotropic trap*, Phys. Rev. A, **69** (2002), article 023618.
- [32] E. POLI, A. LITVINOV, E. CASOTTI, C. ULM, L. KLAUS, M. J. MARK, G. LAMPORESI, T. BLAND AND F. FERLAINO, *Synchronization in rotating supersolids*, Nat. Phys., **21** (2025), 1820–1825.
- [33] M. SCHMITT, M. WENZEL, F. BÖTTCHER, I. FERRIER-BARBUT AND T. PFAU, *Self-bound droplets of a dilute magnetic quantum liquid*, Nature, **539** (2016), 259–262.
- [34] J. SHEN, T. TANG AND L.-L. WANG, *Spectral Methods: Algorithms, Analysis and Applications*, Springer, 2011.
- [35] Q. SHU, Q. TANG, S. ZHANG AND Y. ZHANG, *A preconditioned Riemannian conjugate gradient method for computing the ground states of arbitrary-angle rotating Bose-Einstein condensates*, J. Comput. Phys., **512** (2024), article 113130.
- [36] J. STUHLER, A. GRIESMAIER, T. KOCH, M. FATTORI AND T. PFAU, *Magnetostriction in a degenerate quantum gas*, J. Magn. Magn. Mater., **316** (2007), 429–432.
- [37] Q. TANG, N. MAUSER AND Y. ZHANG, *A robust and efficient numerical method to compute the dynamics of the rotating two-component dipolar Bose-Einstein condensates*, Comput. Phys. Commun., **219** (2017), 223–235.
- [38] L. TANZI, E. LUCIONI, F. FAMÀ, J. CATANI, A. FIORETTI, C. GABBANINI, R. N. BISSET, L. SANTOS, AND G. MODUGNO, *Observation of a Dipolar Quantum Gas with Metastable Supersolid Properties*, Phys. Rev. Lett., **122** (2019), article 130405.
- [39] F. VICO, L. GREENGARD AND M. FERRANDO, *Fast convolution with free-space Green's functions*, J. Comput. Phys., **323** (2016), 191–203.
- [40] L. WEI AND Y. ZHANG, *Novel compact splitting Fourier spectral method to compute the dynamics of rotating spin-orbit coupled spinor Bose-Einstein condensates*, preprint.
- [41] S. J. WOO, S. CHOI AND N. P. BIGELOW, *Controlling quasiparticle excitations in a trapped Bose-Einstein condensate*, Phys. Rev. A, **72** (2005), article 021605(R).
- [42] Y. ZHANG, *Fast evaluation of convolution-type nonlocal potential*, Mathematica Numerica Sinica, **45**(4) (2023), 385–400.
- [43] T. ZHANG AND F. XUE, *A new preconditioned nonlinear conjugate gradient method in real arithmetic for computing the ground states of rotational Bose-Einstein condensate*, SIAM J. Sci. Comput., **46** (2024), A1764–A1792.